Journal of
Materials Chemistry A

Accepted Manuscript

This article can be cited before page numbers have been issued, to do this please use: Y. Zhou, J. Lu, C. Deng, H. Zhu, G. Z. Chen, S. Zhang and X. Tian, *J. Mater. Chem. A*, 2016, DOI: 10.1039/C6TA03440C.

ROYAL SOCIETY OF CHEMISTRY

www.rsc.org/materialsA

View Article Online
DOI: 10.1039/C6TA03440C

Journal Name

ARTICLE

Nitrogen-doped graphene guided formation of monodisperse microspheres of $LiFePO_4$ nanoplates as the positive electrode material of lithium-ion batteries

Received 00th January 20xx,
Accepted 00th January 20xx

DOI: 10.1039/x0xx00000x

www.rsc.org/

Yingke Zhou[a,*], Jiming Lu[a], Chengji Deng[a], Hongxi Zhu[a], George Z. Chen[a,b], Shaowei Zhang[a] and Xiaohui Tian[a]

Three-dimensional porous composite microspheres of $LiFePO_4$ and nitrogen doped graphene have been synthesized by a solvothermal process coupled with subsequent calcination. The morphologies and microstructures of the composites are investigated by scanning electron microscopy, X-ray diffraction, transmission electron microscopy and X-ray photoelectron spectroscopy. The electrochemical properties are evaluated by constant current charge/discharge tests, cyclic voltammetry and electrochemical impedance spectroscopy. The unique porous structure of the microspheres is constructed by the assembly of nitrogen-doped graphene and $LiFePO_4$ nanoplates, and can remarkably enlarge the electrode/electrolyte interface area, facilitate the electron transfer process, shorten the ionic diffusion path and accelerate the ionic transport throughout the electrode. In electrochemical measurements of specific charge capacity, rate capability and cycling stability, the obtained porous composite microsphere materials offer remarkably promising results for application in high-performance lithium-ion power batteries.

1. Introduction

Lithium ion batteries (LIB) have been widely used in portable electronic devices in our daily life.[1-3] However, further improvements on power and energy density of the current LIB are still needed to meet the demand of wide application in electric vehicles and hybrid electric vehicles.[4-6] The performances and costs of LIB are greatly dependent on the positive electrode materials. Since reported in 1997,[5] $LiFePO_4$ (LFP) has been considered to be a promising positive electrode material and has been widely investigated in the past decade due to its relatively satisfactory theoretical capacity (170 mAh g^{-1}), long cycle life, low raw material cost, high safety and non-toxicity.[2,5,6] Nevertheless, the electrochemical performances of LFP are heavily limited by the inherent sluggish kinetics originated from its low electronic and ionic conductivity.[6,7] Numerous efforts have been tried to overcome these limitations of LFP by doping alien atoms,[8,9] decreasing the particle size,[10,11] optimizing the morphology,[2,3,7,12] and adding conductive phases.[2,13,14] Though decreasing the LFP particle size to nanoscale has been demonstrated to be effective to improve its specific capacity, relatively low tap density and volumetric energy density are usually obtained, and the nanoscale materials tend to agglomerate and show poor thermal and poor cycling stability during long-term uses.[7] In contrast with nanoparticles, three-dimensional (3D) porous LFP microspheres composed of nanosized primary particles have attracted great attentions in recent years because the micron-sized spherical particles exhibit high tap density, whilst the porous and nanosized features are accessible to the electrolyte. Therefore excellent electrode performances in terms of specific capacity, volumetric energy density and power density have been achieved.[2,7,15,16]

Recently, many studies have been reported on the improvement of electrochemical performance of LFP by the addition of conductive carbon nanomaterials, such as carbon black, carbon nanotube (CNT) and graphene.[2,7,16] Especially, when nitrogen doped nanocarbons are applied, further performance improvements of LFP are also reported.[14,17-19] Generally, nitrogen doping can enhance the electronic conductivity of nanocarbon, because the dopants provide more electron carriers in the conduction band.[3,19,20] Moreover, the introduced nitrogen-containing function groups can enhance the wettability and affinity of nanocarbon to electrolyte, prevent LFP aggregation, decrease the activation energy and improve the lithium ion diffusion kinetics.[20] Due to their unique structure and physicochemical properties, nitrogen doped graphenes are an effective additive to electrode materials for performance improvement.[8,14]

[a] The State Key Laboratory of Refractories and Metallurgy, College of Materials and Metallurgy, Wuhan University of Science and Technology, Wuhan 430081, P. R. China. E-mail: zhouyk888@hotmail.com.
[b] Department of Chemical and Environmental Engineering, Faculty of Engineering, University of Nottingham, Nottingham NG7 2RD, UK.

† Electronic Supplementary Information (ESI) available. See DOI: 10.1039/x0xx00000x

View Article Online
DOI: 10.1039/C6TA03440C

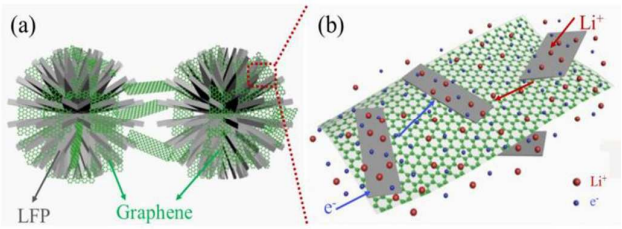

Fig. 1 Schematic illustrations of (a) the microstructure of porous $LiFePO_4$ and nitrogen doped graphene composite microspheres and (b) an enlarged region depicting the mechanisms of accelerated electron transport and Li^+ ion diffusion.

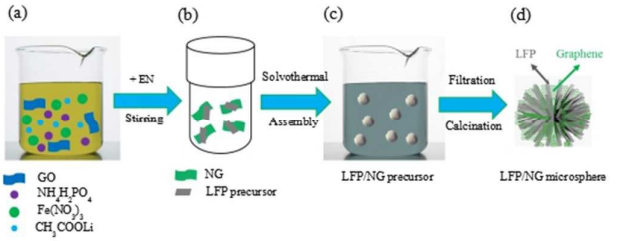

Fig. 2 Depiction of the synthesis process of porous $LiFePO_4$ and nitrogen doped graphene composite microspheres: (a) The dispersion of the raw materials and GO; (b) The solvothermal reaction in an autoclave; (c) The assembled microsphere precursor; (d) The obtained porous $LiFePO_4$ and nitrogen doped graphene composite microspheres after calcination.

In this work, we synthesized novel porous composite microspheres of LFP and nitrogen doped graphene by a solvothermal method coupled with subsequent calcination. During the solvothermal reaction process, anhydrous ethylenediamine (EN) was used and played an important role, which not only served as nitrogen source for doping the graphene, but also assisted the formation of the plate-like LFP in the produced composite microspheres.[7] As illustrated in Fig. 1, the composite microsphere is assembled by the firm contact and connection of LFP nanoplates and nitrogen doped graphene nanosheets which form a 3D conductive network to connect LFP nanoplates and even the individual microspheres. Compared to the recently reported sandwich-like LFP/graphene structure,[21] where thin LFP nanoplates shorten the channels for fast Li ion supply and graphene facilitates fast electron transfer, the present composite microsphere might be assigned to a dual-structure model of layered model and mixed model.[22] The nitrogen doped graphene nanosheets not only overlap the LFP nanoplates (as the layered model), but also crosslink with each other, to build a 3D conductive porous network (similar to the mixed model).[21-23] The electrical contact and conductivity can be improved, and the overall porous structure is beneficial to increase the electrode/electrolyte interface area and provide more paths for Li ion transport. In addition, the composite microsphere composed of LFP nanoplates can shorten the ionic diffusion path and remain stable during charge/discharge cycling.[7,11] Due to these unique and novel structures, the porous microspheres composed of LFP nanoplate and nitrogen doped graphene are expected to present a superior overall performance in terms of specific capacity, rate capability and cyclic stability, and promise an excellent positive electrode material for high performance lithium-ion power batteries.

2. Experimental

2.1 Synthesis of graphene oxide

Graphene oxide (GO) was prepared by a modified Hummers method as reported previously. The main paragraph text follows directly on here.Graphene oxide (GO) was prepared by a modified Hummers method as reported previously.[24] Firstly, flaky graphite powder (5 g) and $NaNO_3$ (3.75 g) were slowly added into 170 ml concentrated H_2SO_4 (98 wt.%) and stirred for 24 h. Then 22.5 g of $KMnO_4$ was gradually added into the solution with an ice-water bath and further stirred for five days. After that, 500 ml of H_2SO_4 solution (5 wt.%) was slowly added into the mixture, and then 45 ml of H_2O_2 (30 wt.%) was added and the solution was stirred for 2 h. Finally, 2 L aqueous solution containing 30 wt.% H_2SO_4 and 1 wt.% H_2O_2 was used to wash the suspension by a centrifuge for several times, and then plenty deionized water was used to further wash until the pH value close to 7.

2.2 Synthesis of porous LFP and nitrogen doped graphene composite microspheres

The porous LFP and nitrogen doped graphene composite microspheres were synthesized by a solvothermal process and the subsequent calcination, as schematically illustrated in Fig. 2. Briefly, 0.02 mol of $CH_3COOLi{\cdot}2H_2O$, $Fe(NO_3)_3{\cdot}9H_2O$, $NH_4H_2PO_4$ and 100 mg of GO were first dissolved in 70 mL deionized water. Then, 5 mL of ethylene glycol (EG) and 5 ml of anhydrous ethylenediamine (EN) were separately added to the solution and kept vigorous string for 30 min. After that, the solution mixture was transferred into a 100 mL Teflon-lined autoclave, heated at 180 ^{o}C for 3 h and cooled down to room temperature naturally. The obtained precursor was calcined at 600 ^{o}C for 12 h under the mixed atmosphere of Ar and H_2 (with a volume ratio Ar : H_2 =90 : 10). The obtained porous LFP and nitrogen doped graphene composite microsphere was noted as LFP/NG. For comparison, two other samples were also synthesized by the similar procedures except for the absence of both GO and EN (noted as LFP) or EN (noted as LFP/G).

2.3 Morphology and structure characterization

The morphologies of the LFP composite materials were investigated by a scanning electron microscopy (SEM, PHILIPS XL30TMP) with an acceleration voltage of 15 kV. X-ray powder diffraction (XRD) was carried out by using an Xpert Pro MPD diffractometer with Cu K_α radiation (λ=0.15418 nm) and the diffraction data was collected for 2ϑ angles from 15° to 85°. The microstructures of the LFP composites were investigated by a transmission electron microscopy (TEM, FEI Tecnai G20) at an acceleration voltage of 200 kV and the element distributions were explored by the energy dispersive X-ray spectroscopy (EDX, OXFORD IET200). X-ray photoelectron spectroscopy (XPS) analysis was conducted on a VG Multilab 2000 apparatus. Raman spectra were recorded at room temperature on an IVNIA spectroscopy with an argon ion laser operating at 514 nm. Thermogravimetric analysis (TG) was performed using a Pyris Diamond TG/DTA instrument (STA449/6/G,

View Article Online
DOI: 10.1039/C6TA03440C

NETZSCH) in an oxygen atmosphere. The samples were heated from 100 °C to 1000 °C at a rate of 10 °C min^{-1}. The nitrogen sorption was performed using an Autosorb-1-MP/LP analyzer (Quantachrome, U.S.A). The Brunauere-Emmette-Teller (BET) method was utilized to calculate the specific surface area (S_{BET}). Pore size distributions were derived from the adsorption branches of the isotherms using the Barrette-Joynere-Halenda (BJH) model.

2.4 Electrochemical measurements

The electrochemical performance measurements were carried out using a NEWARE BTS (5 V, 50 mA) computer-controlled battery test system over the voltage range of 2.5–4.0 V at different rates at room temperature with the coin shape half cells. For preparation of the positive electrode, the active material (LFP), acetylene black and PVDF were mixed with a weight ratio of 80:12:8, and the mixture was dispersed into N-methyl-pyrrolidone (NMP) with magnetic stirring for 12 h to obtain the slurry. The resultant slurry was then uniformly pasted on an Al foil and dried at 60 °C for 10 h in a vacuum oven, and the mass loading of active material is around 1.2 mg. The coin cells were assembled in a glove box filled with pure argon. The liquid electrolyte was 1 M $LiPF_6$ solution in the solvent mixture of ethylene carbonate (EC)-dimethyl carbonate (DMC) (1:1 in volume) and the microporous polypropylene film (Celgard 2400) was used as the separator. CV tests were conducted using CHI 660D electrochemical workstation between 2.5–4.2 V at various scanning rates, and EIS measurements were performed over the frequency range of 1 MHz and 100 mHz with an applied perturbation signal of 10 mV at room temperature.

3. Results and discussion

3.1 Structure and morphology

The phase composition and crystal structure of the synthesized LFP positive electrode materials are investigated by XRD measurements, and the diffraction patterns are shown in Fig. 3a. All the patterns can be indexed as orthorhombic olivine phase (JCPDS No. 83-2092),[25,26] and there are no other impurities appeared in the XRD patterns, implying that well crystallized pure-phase LFP microspheres have been obtained. The carbon phase is not found for the relatively low content of graphene. Pure LFP displays sharper and stronger diffraction peaks than the other two samples, and LFP/NG shows the weakest and widened diffraction peaks, suggesting the smallest particle size of this sample. The LFP particle size (*D*) can be calculated by using the following Scherrer equation,

$$D = \frac{k\lambda}{B\cos\theta} \quad (1)$$

Where *k* is Scherrer constant, λ is the X-ray wavelength, *B* is full width at half maximum and θ is the angle of diffraction. The particle sizes of LFP, LFP/G and LFP/NG are calculated to be 45.9, 39.5 and 24.1 nm, respectively, indicating that the addition of graphene and introduction of nitrogen-doping cause obvious decrease of particle size of the active materials, probably due to the varied nucleation and growth environments in these systems. In addition, the preferred orientation can be confirmed from the diffraction peak intensity ratio of $I_{(200)}/I_{(020)}$. Generally, a higher ratio of $I_{(200)}/I_{(020)}$ than that of the standard ($I_{(200)}/I_{(020)}$=2.1) suggests the LFP nanoplates growing preferentially along the *ac* facet.[11,27] The

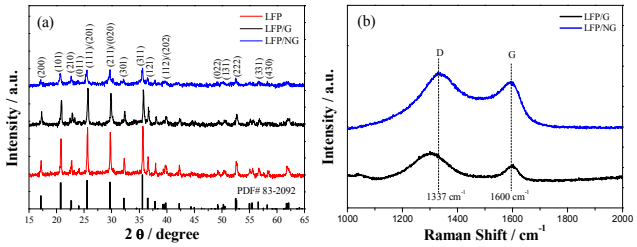

Fig. 3 (a) XRD patterns of LFP, LFP/G and LFP/NG; (b) Raman spectra of LFP/G and LFP/NG.

$I_{(200)}/I_{(020)}$ ratio of LFP/NG is calculated to be 2.3, implying that the growth orientation of LFP nanoplate is along the *ac* plane.

Raman spectroscopy was used to analyze the structure of carbon which was not detected by XRD, and the results are shown in Fig. 3b. The bands observed at 1337 and 1600 cm^{-1} are respectively attributed to the D band and G band, where G band is ascribed to the vibration mode of graphitic carbon and D band is due to the disorders or defects in carbon.[3,13,28] The intensity ratio of D band and G band (I_D/I_G) stands for the degree of surface disorder of carbon materials.[3,28] The I_D/I_G values of LFP/G and LFP/NG are calculated to be 1.19 and 1.21, respectively. LFP/NG shows higher I_D/I_G value than LFP/G, suggesting that more structural defects have been introduced after N-doping, which is consistent with the previously reported N-doped graphene.[3,29] In comparison to LFP/G, both bands of LFP/NG slightly shift to lower frequencies implying good electronic contact and interaction between LFP and NG.[3,30] In addition, thermogravimetric analysis (Fig. S1) indicates that the weight fraction of carbon in LFP/NG is ~6.2 wt%, which is higher than that of LFP/G (~1.3 wt%). The carbon content of LFP/G could be ascribed to the presence of graphene, while the excessive carbon of LFP/NG might be caused by the decomposition of EN. The organic residual carbon may coat on the local conductive paths in individual LFP particles and could assist the nitrogen doped graphene to form an entire 3D conductive network for LFP active materials.[20]

SEM imaging was conducted to investigate the microstructure of the samples, and the typical low and high resolution SEM images are displayed in Fig. 4. The low resolution SEM images (Fig. 4a, c, e) show that all the three samples are assembled into uniform 3D porous microspheres with an average diameter of about 2 μm. Graphene is hardly observed from the SEM images owing to the resolution limitation. As shown in Fig. 4a-d, the microspheres of LFP and LFP/G are composed of irregular nanoparticles with an average diameter of 200 nm. As depicted in Fig. 4e and f, the LFP/NG microspheres are composed of interconnected nanoplates with an average thickness of around tens of nanometers and plane size of hundreds of nanometers. Therefore, the LFP/NG microspheres present looser and more open porous structure in comparison to LFP and LFP/G, which might be beneficial to enlarge the electrode/electrolyte interfacial area and shorten the lithium ion diffusion path.[4] The overall porous characteristics of LFP, LFP/G and LFP/NG could be formed with the assistance of EG, while the different morphologies between LFP/NG and the other two samples might be ascribed to the effects of ethylenediamine added in the

View Article Online
DOI: 10.1039/C6TA03440C

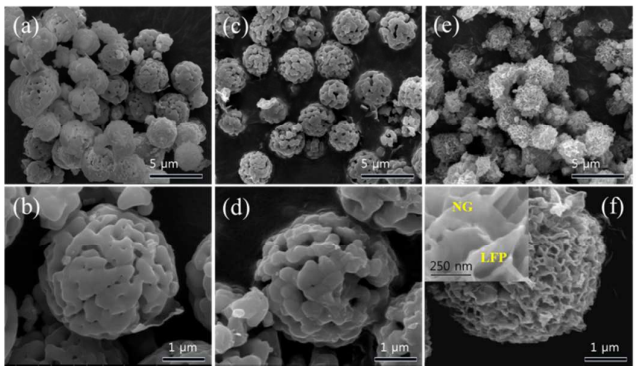

Fig. 4 Low and high-resolution SEM images of (a, b) LFP, (c, d) LFP/G and (e, f) LFP/NG. Inset: high-resolution SEM image revealing the nanoplate morphology of LFP/NG.

reaction system. Ethylenediamine could decompose and induce doping of graphene with nitrogen to introduce N-containing functional groups, which act as nucleation sites for LFP deposition, control the crystal growth and prevent aggregation of LFP particles.[14,20] In addition, for the strong complexing ability, ethylenediamine may complex with iron ions and further impact the crystal growth of LFP.[7]

TEM measurements were conducted to further investigate the morphology and microstructure of LFP porous composite microspheres, and the typical results are shown in Fig. 5. Both LFP and LFP/G samples display dense microspheres composed of LFP nanoparticles (Fig. 5a,b), while LFP/NG presents loose and open porous structure composed of interwoven nanoplates (Fig. 5c), which are consistent with the previous SEM investigations. As marked in Fig. 5b and c, the composited graphene or nitrogen-doped graphene sheets could be clearly observed, which form a distinctive conducting network and may provide more paths to facilitate the charge transfer. The high-resolution TEM images and corresponding selected area electron diffraction patterns (SEAD) of LFP/NG are shown in Fig. 5d-g. As marked in Fig. 5d and f, LFP displays a nanoplate structure with the thickness of around 38.1 nm and the plane size of hundreds of nanometers, and which is uniformly coated by the continuous conductive networks of nitrogen doped graphene. The tight contact between LFP nanoplates and graphene networks could improve electron transfer and the electrochemical Li-insertion performance.[4] Fig. 5e demonstrates that the LFP nanoplate is highly crystallized and the lattice fringes with the spacing of 0.429 nm correspond to the (101) plane of orthorhombic LFP. The inserted SEAD pattern indicates that the crystallographic facet of the LFP nanoplate is along the (101) plane, and the vertical direction is [010], which is beneficial for shortening the Li^+ diffusion route in LFP crystal.[3,25] Fig. 5f shows the side surface of a LFP nanoplate, and the corresponding SEAD pattern (inset of Fig. 5g) further confirms the preferred crystal orientation as above.[3,11,25,27] The energy dispersive X-ray (EDX) elemental mapping results displayed in Fig. 5f indicate that though the C element imaging is partly interfered by the applied carbon support under TEM investigations, the Fe, P, O, N and C elements are uniformly distributed in the LFP/NG microspheres, implying that well distributed and composited LFP and NG porous microspheres

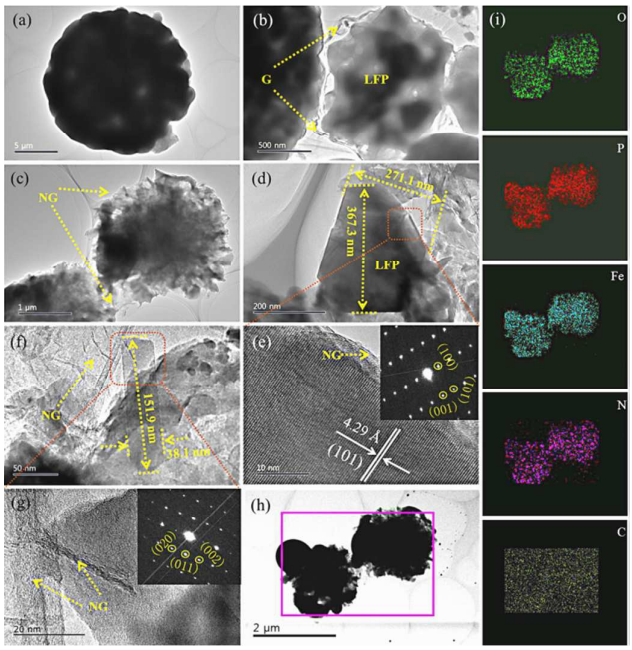

Fig. 5 TEM images of (a) LFP, (b) LFP/G and (c) LFP/NG; (d, e, f, g) High-resolution TEM images and corresponding SEAD patterns of LFP/NG; (h, i) Elemental mapping images of LFP/NG.

have been successfully synthesized.

Fig. 6 shows the nitrogen adsorption and desorption isotherms ofLFP, LFP/G and LFP/NG. The isotherms of LFP and LFP/G could be attributed to a type III curve, implying a macroporous structure is obtained, while that of LFP/NG presents a type IV curve with hysteresis loops, a typical characteristic of mesoporous structure.[7] The measured Brunauer-Emmett-Teller (BET) specific surface areas of LFP, LFP/G and LFP/NG are 2.6, 5.8 and 54.8 $m^2 g^{-1}$, respectively. The corresponding pore-size distribution plots are displayed in Fig. S2. As depicted in Fig. S2a and b, besides the few percent of mesopores below 10 nm, the predominant macroporous structure of LFP and LFP/G could not be correctly detected due to the limitation of porosity analyzer**.** LFP/NG exhibits bimodal porous structure with pore size of 3.8 and 9.6 nm (Fig. S2c), respectively, and the corresponding BJH desorption cumulative pore volume is

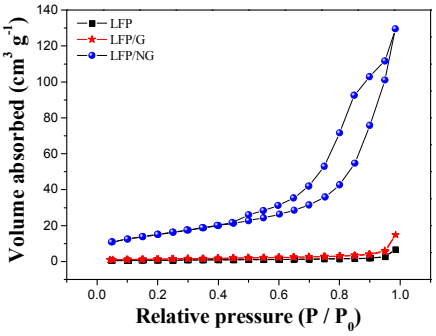

Fig. 6 Nitrogen adsorption and desorption isotherms of LFP, LFP/G and LFP/NG.

View Article Online
DOI: 10.1039/C6TA03440C

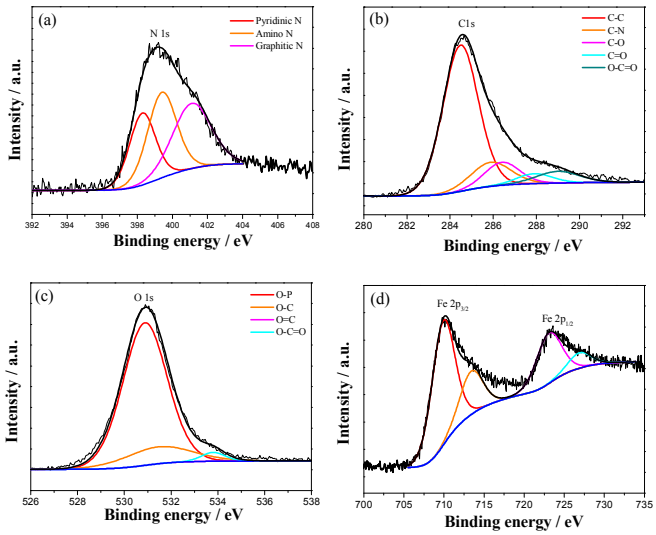

Fig. 7 XPS core-level spectra of LFP/NG: (a) N 1s; (b) C 1s; (c) O 1s; (d) Fe 2p.

0.21 cm^3 g^{-1}, verified the mesoporous characteristic of LFP/NG. The surface area of LFP/NG is remarkably higher than that of LFP and LFP/G, which might be ascribed to the unique open porous composite structure and the small amount of excessive carbon in this sample due to the decomposition of EN, and these results are consisted with the SEM investigation and TGA analysis. The mesoporous structure and high surface area of LFP/NG could be beneficial to enlarge the interfacial area between electrode and electrolyte, and improve the specific capacity and rate capability of the active material.[2,3,31]

XPS measurements were further conducted to analyze the surface elemental composition and electronic state of the as-prepared materials. The core level spectra and deconvolution analysis of N 1s, C 1s, O 1s and Fe 2p of LFP/NG are shown in Fig. 7, and the corresponding peak position, attribution and component of LFP, LFP/G and LFP/NG are summarized in Table 1. The N 1s spectrum in Fig. 7a could be reasonably fitted with three components of pyridine type N (398.3 eV), amino type N (399.4 eV) and graphitic type N (401.1 eV), with the corresponding contents of 27.26%, 36.12% and 36.62%, respectively.[29,32] The high resolution C 1s spectrum in Fig. 7b could be deconvoluted into five peaks at 284.6, 285.9, 286.5, 287.9 and 289 eV, respectively ascribed to C-C, C-N, C-O, C=O and O-C=O.[29,32] As displayed in Table 1, the C-C bond was dominant in the C functional groups, which may contribute to the electronic conductivity improvement of the composite materials.[29] The presence of C-N bond in LFP/NG further proves the formation of N-doping nanocarbon in this sample. The O 1s spectrum could be decomposed into four peaks of O-P, O-C, O=C and O-C=O, located respectively at 530.9, 531.5, 532.6 and 533.8 eV (Fig. 7c).[24] The Fe 2p spectrum in Fig. 7d splits to two peaks due to the spin-orbit coupling, and the peaks located at around 709.9 and 723.0 eV along with two satellite peaks at 713.5 and 727.0 eV are respectively ascribed to Fe $2p_{3/2}$ and Fe $2p_{1/2}$, which are characteristics of Fe^{2+} in the LFP lattice sites.[30] As summarized in the supplementary Table S1, in comparison to the other two samples, the different contents of Fe components of LFP/NG suggest the change of electronic structure when the nitrogen-doped graphene has been introduced, probably due to the enhanced interaction between LFP and nanocarbon and which may contribute to the stability and cycling performance of the composites.

The morphology and structure characterizations described above demonstrate that the three-dimensional porous composite microspheres assembled by LFP nanoplates and NG nanosheets have been successfully synthesized. Regarding the formation mechanism, the presence of ethylenediamine might be a critical condition. In the absence of ethylenediamine, microspheres consisting of nanoparticles instead of nanoplates are formed, as in the case of LFP/G. Ethylenediamine has a stronger chelating ability for transition-metal ions and may have a great effect on the release of isolated iron ions during the solvothermal reaction process,[7] which influences the nucleation and crystal growth of LFP and leads to the formation of nanoplates. The nanoplates may then self-assemble into microspheres driven by the reduction in surface free energy. The introduction of NG might be another reason, as plenty of nitrogen-containing functional groups in NG could impact the nucleation and growth behavior of LFP, and further assist the formation of microspheres by the strong interaction between LFP and NG.

3.2 Electrochemical performance

The charge-discharge tests over the voltage range of 2.5–4.0 V at various rates were conducted to evaluate the electrochemical performances of the as-prepared LFP composite microsphere positive electrode materials. Fig. 8a presents the initial charge-discharge curves of LFP, LFP/G and LFP/NG at the rate of 0.1 C. All the samples exhibit a flat voltage plateau at around 3.45 V corresponding to the Li^+ insertion and extraction process between $FePO_4$ and $LiFePO_4$. At 0.1C, the discharge specific capacities of LFP, LFP/G and LFP/NG are 135.5, 149.5 and 178 mA h g^{-1}, respectively, implying that the specific capacity of LFP is effectively enhanced with the modification of NG conductive network. The discharge specific capacity of LFP/NG is slightly beyond the theoretical capacity of LFP. This is similar to the recently reported LFP/C/graphene composites, and the excess capacity of LFP/NG at 0.1 C could be attributed to the reversible redox reaction between the lithium ions of the electrolyte and the graphene.[33] From the enlarged section inserted in Fig. 8a, the voltage interval values between the charge/discharge plateaus of LFP, LFP/G and LFP/NG are respectively 73, 68 and 53 mV. The smaller voltage interval of LFP/NG indicates the lower polarization than the other two samples during the charge-discharge process, which might be attributed to the facilitated lithium ions diffusion and improved electronic conductivity of the porous LFP/NG composite microspheres. Fig. 8b exhibits the discharge curves of LFP/NG at various rates between 0.1 and 10 C. The specific discharge capacities of LFP/NG are 178, 177.5, 175.9, 159.9, 153.5, 142.8 and 114 mAh g^{-1} at 0.1, 0.2, 0.5, 1, 2, 5 and 10 C, respectively. From Fig. 8b, the discharge curves of LFP/NG are composed of a plateau at around 3.4 V and a sluggish slope between 2.5–3.4 V. Similar discharge profiles have been observed in many LFP/C composites or nanometer-sized LFP.[10,34-37] The occurrence of sluggish slope might be ascribed to the capacitive

View Article Online
DOI: 10.1039/C6TA03440C

behavior of the interfacial lithium storage process, similar to that reported for nanosized transition-metal oxides at low potential.[38,39] When the dimension of active materials approaching the nanoscale, the pseudocapacitive effect may occur at the surface, and the total storage of charge is composed of lithium ion intercalation and capacitive behavior, as the previously reported hierarchically constructed nanoplates.[36,37] The sluggish slope might also be caused by the formation of single-phase solid solution during the discharge process, as the thickness of LFP nanoplate is below the reported critical value (45 nm).[10,40]

Shown in Fig. 8c is the rate performance of LFP, LFP/G and LFP/NG at various charge/discharge rates. When the rate increases, the specific capacity of LFP and LFP/G decreases greatly, while that of LFP/NG remains much higher and relatively stable. For example, at the rate 1 C, low specific capacities of 92 and 107.8 mAh g^{-1} are obtained for LFP and LFP/G, much lower than that of LFP/NG (159.9 mAh g^{-1}), and at the higher rate of 10 C, the superior characteristics of the LFP/NG are even clearer. Compared to the previously reported LFP materials with similar morphologies, LFP/NG also presents a superior specific capacity and rate capability, for example, at the rate of respectively 0.1 C and 10 C, the specific capacities of LFP/NG (178 and 114 mAh g^{-1}) are much higher than those of $LiFePO_4$/C/PPy microspheres (140 and 86 mAh g^{-1}),[7] porous $LiFePO_4$/C microspheres (156.9 and 74 mAh g^{-1}),[41] and interconnected $LiFePO_4$/C microspheres (163.1 and 100.2 mAh g^{-1}) at the same rate.[42] Fig. 8d shows the long-term cyclic performance of the LFP porous composite microsphere materials for over 300 cycles at the 1 C rate. LFP/NG delivers the highest specific capacity during the whole period, and of which the initial capacity is 159.9 mAh g^{-1} and the terminative capacity is 151.9 mAh g^{-1}. Thus, capacity retention of 95% is obtained for LFP/NG after 300 cycles, in contrast to the lower retentions of 90% and 93% for LFP and LFP/G, suggesting the improved cycle reversibility and stability of LFP/NG. The high specific capacity, rate capability and cycling stability of LFP/NG might be originated from the unique open porous microsphere structure, the firm contact and interaction between LFP nanoplates and NG nanosheets, and the resultant superior charge transportation and structure stability of LFP/NG composites.

The cyclic voltammograms (CV) of the LFP composite microsphere at a scan rate of 0.1 mV s^{-1} are shown in Fig. 9a. All electrodes exhibit a pair of symmetrical anodic/cathodic peaks, corresponding to the oxidation/reduction transformation between Fe^{2+} and Fe^{3+}. For LFP/NG, the oxidation peak is located at 3.499 V and the reduction peak is located at 3.352 V, indicating a potential gap of 147 mV. In contrast, the potential gaps of LFP and LFP/G are respectively 304 and 192 mV, higher than that of LFP/NG. This reduced potential interval implies the improved reversibility and reactivity of LFP/NG compared to the other two samples.[8] In addition, higher redox peak current density of LFP/NG is investigated in comparison to that of LFP and LFP/G, which indicates higher Li insertion capacity and is consistent with the previous charge/discharge tests. In order to further examine the reversibility and stability of the LFP/NG electrode during the redox reaction process, the CV curves at different scan rates are acquired and presented in Fig. 9b, and the inserted are results of continuous 20 cycles at the scan rate of 1 mV s^{-1}. The oxidation and reduction

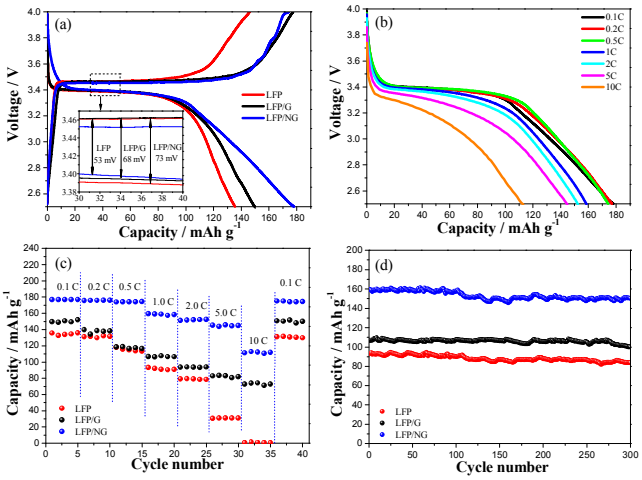

Fig. 8 (a) Initial charge/discharge curves of LFP, LFP/G and LFP/NG at 0.1 C, (b) The discharge curves of LFP/NG at different discharge rates, (c) The rate performances at various discharge rates, and (d) The cycling performances of LFP, LFP/G and LFP/NG during 300 cycles at 1 C.

peaks are highly symmetric at various scan rates and keep nearly unchanged upon multiple cycles, suggesting the remarkable cyclicreversibility and stability of the lithium insertion/extraction reactions within the LFP/NG electrode.[13] Electrochemical impedance spectra are used to further study the reaction kinetics of LFP, LFP/G and LFP/NG electrodes, as displayed in Fig. 9c. The impedance spectra can be reasonably fitted and analyzed according to the inserted equivalent circuit. The high frequency intercept of the semicircle refers to the uncompensated resistance (R_u). The parallel circuit of surface capacitance (C_1) and polarization resistance (R_1) corresponds to electrode roughness, inhomogeneous reaction and solid electrolyte interface film at the surface. The semicircle corresponds to the double-layer capacitance (CPE) and the charge transfer resistance (R_2) between the interface of electrode and electrolyte, and the straight line at low frequency is ascribed to Warburg resistance (Z_w) associated with ion diffusion within the electrode.[2,13] The fitting results are summarized in Table 2. LFP/NG presents slightly decreased Ru and greatly reduced R_1 and R_2 in comparison to those of LFP and LFP/G, indicating the remarkably improved charge transfer and reaction kinetics by the modification with nitrogen doped graphene and formation of open porous microsphere structure. On the basis of the inclined line in the Warburg region, the Li^+ diffusion coefficient (D / cm^2 s^{-1}) can be calculated using the following equation:[2,8]

$$D = \frac{R^2T^2}{2A^2n^4F^4C^2\sigma^2} \quad (2)$$

Where R is the gas constant, T is the absolute temperature, A is the surface area of the electrode, n is the number of electron per molecule during redox reaction (n=1 for the redox of Fe^{3+}/Fe^{2+}), F is the Faraday constant, C is the concentration of lithium-ion (7.69×10^{-3} mol cm^{-3}), and σ is the Warburg factor associated with the negative imaginary part of impedance ($-Z_{im}$ / Ω) and ω (frequency, Hz) according to the following equation:[2,6,8]

$$-Z_{im} = k + \frac{\sigma}{\sqrt{\omega}} \quad (3)$$

View Article Online
DOI: 10.1039/C6TA03440C

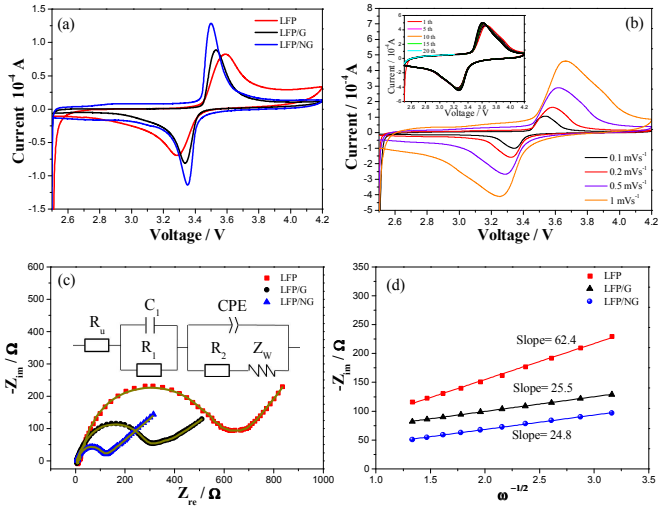

Fig. 9 CV curves of LFP, LFP/G and LFP/NG at a scan rate of 0.1 mV s^{-1}, (b) CV curves of LFP/NG at different scan rates, and the inserted curves of continuous 20 cycles at 1 mV s^{-1}, (c) EIS profiles and fitting curves of LFP, LFP/G and LFP/NG, the inset is the applied equivalent circuit, and (d) The fitting curves of $-Z_{im}$ and the reciprocal square root of the angular frequency at low frequency region of LFP, LFP/G and LFP/NG.

Where *K* is a constant. From equation 3, the Warburg factor σ can be obtained by linearly fitting the plot between $-Z_{im}$ and the reciprocal square root of the angular frequency (as shown in Fig.9d and supplementary Table S2). Then according to equation 2, the lithium ion diffusion coefficients of LFP, LFP/G and LFP/NG are calculated to be 6.25×10^{-14}, 3.75×10^{-13} and 3.99×10^{-13} cm^2 s^{-1}, respectively, which are comparable to the previously reported values.[2,8] As listed in Table 2, the LFP/NG electrode demonstrates much higher Li^+ diffusion coefficient and lower impedance than those of LFP, and even LFP/G electrode, which are attributed to the shortened ion diffusion route from the unique LFP nanoplate structure, the increased electrode/electrolyte contact area from the constructed porous microsphere structure, and the improved electronic conductivity by the introduction of nitrogen doped graphene. The reduced charge transfer impedance and increased Li^+ diffusion coefficient of LFP/NG significantly favor its superior specific capacity, rate characteristic as well as cycling stability.

4. Conclusions

In summary, we have reported the successful synthesis of porous composite microspheres of LFP and nitrogen doped graphene using a solvothermal method coupled with high-temperature calcination. The porous composite microspheres are composed of firmly connected LFP nanoplates and NG nanosheets, and exhibit remarkably enhanced specific capacity, rate characteristic and cyclic stability in comparison to pure LFP and the similar composite with undoped graphene. Such performance improvements are attributable to the unique morphology and structure of the porous composite microspheres, which could greatly enlarge the electrode/electrolyte interface area, reduce the ion diffusion distance and improve the electrochemical accessibility. Moreover, the NG modification could provide nucleation sites for LFP deposition, control the crystal growth, and greatly increase the electrical contact and conductivity. Therefore, the porous composite microsphere is a promising positive electrode material for lithium-ion power battery applications.

Acknowledgements

This work was supported by the National Natural Science Foundation of China (No. 51372178) and the Natural Science Foundation for Distinguished Young Scholars of Hubei Province of China (No. 2013CFA021).

Notes and references

1 M. Armand and J. M. Tarascon, *Nature*, 2008, **451,** 652-657.
2 Y. K. Zhou, J. Wang, Y. Y. Hu, R. O'Hayre and Z. P. Shao, *Chem. Commun.*, 2010, **46,** 7151-7153.
3 B. Wang, W. Al Abdulla, D. L. Wang and X. S. Zhao, *Energy Environ. Sci.*, 2015, **8,** 869-875.
4 W. Wei, D. Z. Chen, R. N. Wang and L. Guo, *Nanotechnology*, 2012, **23,** 475401.
5 A. K. Padhi, J. B. Goodenough and K. S. Nanjundaswamy, *J. Electrochem. Soc.*, 1997, **144,** 1188-1194.
6 L. L. Peng, Y. Zhao, Y. Ding and G. H. Yu, *Chem. Commun.*, 2014, **50,** 9569-9572.
7 C. W. Sun, S. Rajasekhara, J. B. Goodenough and F. Zhou, *J. Am. Chem. Soc.*, 2011, **133,** 2132-2135.
8 B. Wang, B. H. Xu, T. F. Liu, P. Liu, C. F. Guo, S. Wang, Q. M. Wang, Z. G. Xiong, D. L. Wang and X. S. Zhao, *Nanoscale*, 2014, **6,** 986-995.
9 C. M. Ban, W. J. Yin, H. W. Tang, S. H. Wei, Y. F. Yan and A. C. Dillon, *Adv. Energy Mater.*, 2012, **2,** 1028-1032.
10 P. Gibot, M. Casas-Cabanas, L. Laffont, S. Levasseur, P. Carlach, S. Hamelet, J. M. Tarasco and C. Masquelier, *Nature Mater.*, 2008, **7,** 741-747.
11 L. Wang, X. M. He, W. T. Sun, J. L. Wang, Y. D. Li and S. S. Fan, *Nano lett.*, 2012, **12,** 5632-5636.
12 C. M. Doherty, R. A. Caruso, B. M. Smarsly and C. J. Drummond, *Chem. Mater.*, 2009, **21,** 2895-2903.
13 G. Wu, Y. K. Zhou and Z. P. Shao, *Appl. Surf. Sci.*, 2013, **283,** 999-1005.
14 J. P. Jegal, K. C. Kim, M. S. Kim and K. B. Kim, *J. Mater. Chem. A*, 2014, **2,** 9594-9599.
15 J. K. Kim, Crystengcomm, 2014, **16**, 2818-2822.
16 W. Wei, S. Gao, Z. Yang and L. Guo, *Rsc Advances*, 2014, **4**, 56701-56706.
17 B. Zhang, X. B. Yuan, H. Li, X. W. Wang, J. F. Zhang, H. Z. Chen and J. C. Zheng, *J. Alloys Compd.*, 2015, **627,** 13-19.
18 S. Yoon, C. Liao, X. G. Sun, C. A. Bridges, R. R. Unocic, J. Nanda, S. Dai and M. P. Paranthaman, *J. Mater. Chem.*, 2012, **22,** 4611-4614.
19 J. L. Yang, J. J. Wang, X. F. Li, D. N. Wang, J. Liu, G. X. Liang, M. Gauthier, Y. L. Li, D. S. Geng, R. Y. Li and X. L. Sun, *J. Mater. Chem.*, 2012, **22,** 7537-7543.
20 J. J. Wang, X. L. Sun, *Energy Environ. Sci.*, 2015, **8,** 1110-1138.
21 X. Guo, Q. Fan, L. Yu, J. Liang, W. Ji, L. Peng, X. Guo, W. Ding and Y. Chen, *J. Mater. Chem. A*, 2013, **1**, 11534-11538.
22 Z. S. Wu, G. Zhou, L. C. Yin, W. Ren, F. Li and H.-M. Cheng, *Nano Energy*, 2012, **1**, 107-131.

View Article Online
DOI: 10.1039/C6TA03440C

23 Y. Zhang, H. Zhang, X. Li, H. Xu and Y. Wang, *Nanotechnology*, 2016, **27**, 155401.
24 J. M. Lu, Y. K. Zhou, T. T. Jiang, X. H. Tian, X. F. Tu and P. C. Wang, *Ceram. Int.*, 2016, **42,** 1281-1292.
25 S. Yang, X. Zhou, J. Zhang and Z. Liu, *J. Mater. Chem.*, 2010, **20**, 8086.
26 K. Saravanan, M. V. Reddy, P. Balaya, H. Gong, B. V. R. Chowdari and J. J. Vittal, J. Mater. Chem., 2009, **19**, 605-610.
27 B. Wang, A. Liu, W. Al Abdulla, D. Wang and X. S. Zhao, Nanoscale, 2015, **7**, 8819-8828.
28 K. Bazzi, B. P. Mandal, M. Nazri, V. M. Naik, V. K. Garg, A. C. Oliveira, P. P. Vaishnava, G. A. Nazri and R. Naik, *J. Power Sources*, 2014, **265**, 67-74.
29 X. Xu, Y. Zhou, J. Lu, X. Tian, H. Zhu and J. Liu, *Electrochim. Acta*, 2014, **120**, 439-451.
30 Y. Chang, J. Li, B. Wang, H. Luo, H. He, Q. Song and L. Zhi, *J.mater.chem.a*, 2013, **1**, 14658-14665.
31 C. M. Doherty, R. A. Caruso and C. J. Drummond, *Energy Environ. Sci.*, 2010, **3**, 813-823.
32 J. Lu, Y. Zhou, X. Tian, X. Xu, H. Zhu, S. Zhang and T. Yuan, *Appl. Surf. Sci.*, 2014, **317**, 284-293.
33 B. Lung-Hao Hu, F. Y. Wu, C. T. Lin, A. N. Khlobystov and L. J. Li, *Nat. Commun.*, 2013, **4**, 1687.
34 Y. Wang, Y. Wang, E. Hosono, K. Wang and H. Zhou, *Angew. Chem.*, 2008, **47**, 7461-7465.
35 C. M. Doherty, R. A. Caruso, B. M. Smarsly, P. Adelhelm and C. J. Drummond, *Chem. Mater.*, 2009, **21**, 5300-5306.
36 X. L. Wu, L. Y. Jiang, F. F. Cao, Y. G. Guo and L. J. Wan, *Adv. Mater.*, 2009, **21**, 2710-2714.
37 H. Yang, X. L. Wu, M. H. Cao and Y. G. Guo, *J. Phys. Chem. C*, 2009, **113**, 3345-3351.
38 P. Balaya, H. Li, L. Kienle and J. Maier, *Adv. Funct. Mater.*, 2003, **13**, 520-531.
39 Y. S. Hu, L. Kienle, Y. G. Guo and J. Maier, *Adv. Mater.*, 2006, **18**, 1421-1426.
40 N. Meethong, H.-Y. S. Huang, W. C. Carter and Y.-M. Chiang, *Electrochem. and Solid-State Lett.*, 2007, **10**, A134.
41 L. Ni, J. Zheng, C. Qin, Y. Lu, P. Liu, T. Wu, Y. Tang and Y. Chen, *Electrochim. Acta*, 2014, **147**, 330-336.
42 D. W. Xu, X. D. Chu, Y. B. He, Z. J. Ding, B. H. Li, W. J. Han, H. D. Du and F. Y. Kang, *Electrochim. Acta*, 2015, **152,** 398-407.